A Photometric Study of the Eclipsing Binary BO Leporis

Edward J. Michaels

Waffelow Creek Observatory, 10780 FM 1878, Nacogdoches, TX 75961; astroed@ejmj.net

Abstract   Multi-band photometric observations of the Algol-type binary BO Lep are presented. The visual light curve displays a 1.7-magnitude deep primary eclipse and a shallow 0.2-magnitude secondary eclipse. Photometric light curve solutions were obtained using the Wilson-Devinney program which describe a semidetached configuration with a mass ratio of $M_2/M_1 = 0.510$, an inclination of $i = 86.7°$, and a temperature difference of $\Delta T = 2042$ K between the F2 and K3 component stars. The filling factor for the primary star is 72% and 99% for the secondary. A small asymmetry in the light curves was modeled with a cool spot located on the secondary star. New linear and quadratic ephemerides were computed, giving an orbital period of 0.80625824 d that is decreasing at a rate of -1.55×10^{-7} d yr^{-1}.

1. Introduction

The variability of BO Lep (GSC 05352-00074, TYC 5352-74-1) was first seen in sky patrol plates taken at the Bamberg Southern Station (Strohmeier 1967). More recent surveys have also identified the changing light of this star. These include the Northern Sky Variability Survey (NSVS), the All-Sky Automated Survey (ASAS), and the Catalina Sky Surveys (CSS) (Woźniak *et al.* 2004; Pojmański 2002; Drake *et al.* 2014). BO Lep was included in a catalog (compiled from CSS data) of northern eclipsing binaries with Algol-type light curves (Papageorgiou *et al.* 2018). This catalog gives an orbital period of 0.8062561 d and an eclipse amplitude of 1.405 magnitude. Using machine-learning algorithms Papageorgiou *et al.* (2018) classified each cataloged EA-type eclipsing binary as detached (D) or semidetached (SD). Of the 4,050 stars in the catalog (their Table 1), 4% received an uncertain classification (D/SD). BO Lep was in this group.

Eclipsing binary stars provide a means for determining fundamental stellar properties if accurate measurements are available. In this paper a photometric study of BO Lep is presented using precision high cadence observations. The observations and data reduction methods are presented in section 2. A period analysis is presented in section 3. Analysis of the light curves using the Wilson-Devinney model is presented in section 4. Discussion of the results is presented in section 5, and conclusions are presented in section 6.

2. Photometric observations

Photometric observations were acquired at the Waffelow Creek Observatory, Nacogdoches, Texas, using a 0.36-m Ritchey-Chrétien robotic telescope and a SBIG-STXL camera with a cooled KAF-6303E CCD ($-20°$ C, 9-µm pixels). This data was collected on 17 nights in November and December 2021 and January 2022. Images were obtained in four passbands each night: Johnson V and Sloan g', r', and i'. The observation dates and number of images acquired are shown in the observation log (Table 1). The images were calibrated using bias, dark, and flat frames. MIRA software (Mirametrics 2015) was used for image calibration and the ensemble differential aperture photometry of the light images. The locations of the comparison

and check stars are shown in Figure 1, and Table 2 gives their coordinates and standard magnitudes. The first comparison star in Table 2 (C1, GSC 05352-00056) is located only 19.4" to the SE of BO Lep and is approximately the same brightness. Each night, the seeing profile of these two stars was checked to verify that there was no blending of light in the sky and target annuli. It is interesting to note that the proper motion of these two stars is nearly the same in both R. A. and Dec. (EDR3 data; Gaia Collaboration *et al.* 2021). Gaia parallaxes

Table 1. Observation log.

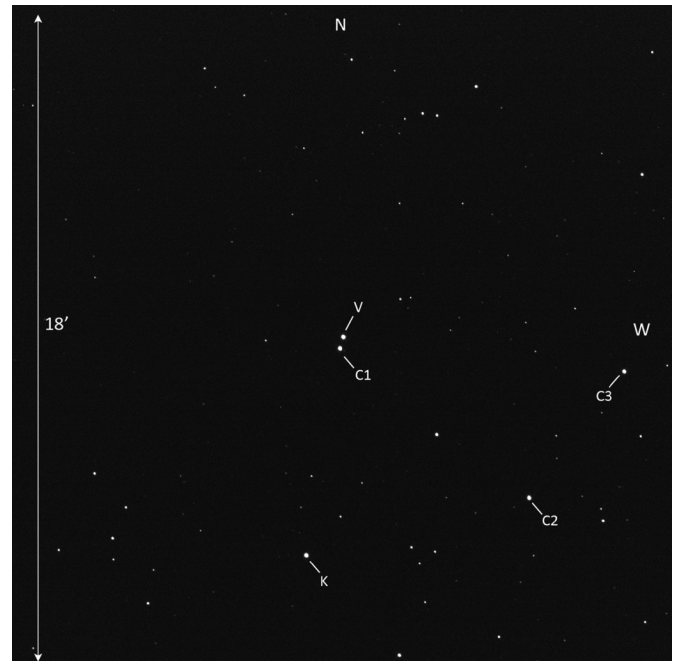| Filter	Dates	No. Nights	No. Images
V, g', r', i'	2021 Nov 4–7	4	966
V, g', r', i'	2021 Nov 11–15	5	1217
V, g', r', i'	2021 Nov 22, 23, 29, 30	4	875
V, g', r', i'	2021 Dec 11, 12	2	478
V, g', r', i'	2022 Jan 16, 17	2	496

Figure 1. Finder chart for BO Lep (V), comparison (C1, C2, and C3) stars, and check (K) stars.

Table 2. APASS comparison and check star magnitudes.

Star	R. A. (2000) h	Dec. (2000) °	V	g'	r'	i'
BO Lep	5.880978	−11.05331	—	—	—	—
GSC 05352-00056 (C1)	5.881077	−11.05811	11.551	11.992	11.420	11.241
GSC 05352-00007 (C2)	5.875297	−11.12670	11.710	12.040	11.590	11.412
GSC 05325-00042 (C3)	5.882182	−11.15182	11.639	11.969	11.511	11.329
GSC 05325-00062 (K)	5.893910	−11.18185	11.541	11.848	11.378	11.292
Standard deviation of K-star magnitudes			± 0.006	± 0.007	± 0.006	± 0.006

Table 3. Average light-curve properties.

|	Min I Mag.	Min II Mag.	Δ Mag. Min II − Min I	Max I Mag.	Max II Mag.	Δ Mag. Max II − Max I	Mag. Range Max II − Min I
V	12.954 ± 0.003	11.475 ± 0.005	1.479 ± 0.006	11.246 ± 0.003	11.250 ± 0.002	0.003 ± 0.004	1.705 ± 0.004
g'	13.420 ± 0.002	11.730 ± 0.001	1.689 ± 0.003	11.524 ± 0.001	11.527 ± 0.003	0.003 ± 0.003	1.893 ± 0.004
r'	12.715 ± 0.003	11.436 ± 0.003	1.279 ± 0.004	11.177 ± 0.002	11.181 ± 0.003	0.005 ± 0.004	1.533 ± 0.004
i'	12.409 ± 0.002	11.350 ± 0.003	1.059 ± 0.003	11.048 ± 0.002	11.055 ± 0.003	0.007 ± 0.003	1.354 ± 0.004
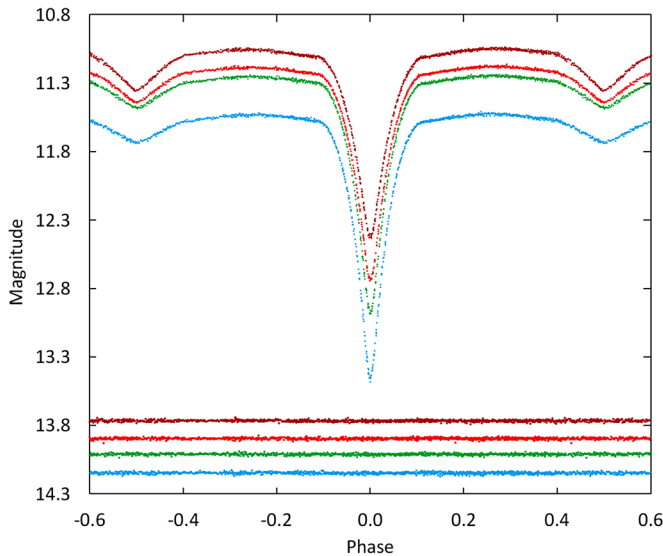
Figure 2. The folded CCD light curves in standard magnitudes. From top to bottom the passbands are i', r', V, and g'. In the same order, the bottom curves are the check-star magnitudes with offsets of +2.5, +2.5, +2.3, and +2.5 magnitudes, respectively. Error bars were omitted from the plotted points for clarity.

Table 4. Times of minima and O − C residuals.

Method	Epoch HJD 2400000+	Error	Cycle No.	O − C	Reference
ccd	51534.7138	0.0008	−2313.0	−0.00172	1
ccd	51535.1138	0.0032	−2312.5	−0.00494	1
ccd	52067.6529	0.0018	−1652.0	0.00150	1
ccd	52068.0543	0.0021	−1651.5	−0.00029	1
ccd	52810.2156	0.0011	−731.0	0.00147	1
ccd	52810.6169	0.0016	−730.5	−0.00034	1
ccd	53399.5880	—	0.0	0.00000	2
ccd	53624.5390	0.0018	279.0	0.00529	1
ccd	* 53624.9272	0.0051	279.5	−0.00966	1
ccd	54343.7170	0.0014	1171.0	0.00206	1
ccd	* 54344.1134	0.0171	1171.5	−0.00471	1
ccd	54538.0225	—	1412.0	−0.00041	3
ccd	54863.7504	0.0001	1816.0	−0.00031	4
ccd	54884.7161	0.0006	1842.0	0.00272	1
ccd	* 54885.1012	0.0168	1842.5	−0.01536	1
ccd	55528.9207	0.0004	2641.0	0.00796	5
ccd	55958.6515	0.0007	3174.0	0.00378	6
ccd	56265.8354	0.0005	3555.0	0.00377	7
ccd	56658.4813	0.0004	4042.0	0.00253	1
ccd	59523.9169	0.0001	7596.0	0.00075	8
ccd	59532.7858	0.0001	7607.0	0.00083	8
ccd	59548.9110	0.0001	7627.0	0.00086	8
ccd	59561.8112	0.0001	7643.0	0.00098	8
ccd	59597.6910	0.0006	7687.5	0.00231	8

*Outliers not used in the period analysis. References: (1) Zasche et al. (2014);
(2) Watson et al. (2014); (3) Papageorgiou et al. (2018); (4) Diethelm (2009);
(5) Diethelm (2011); (6) Diethelm (2012); (7) Diethelm (2013); (8) this paper.*

indicate BO Lep is 104 pc closer (Bailer-Jones *et al.* 2021), thus the pair is an optical double. The standard magnitudes of the comparison stars were taken from the AAVSO Photometric All-Sky Survey database (APASS; Henden *et al.* 2015). The instrumental magnitudes were converted to standard magnitudes using the APASS comparison star magnitudes. The Heliocentric Julian Date (HJD) of each observation was converted to orbital phase (φ) using the following epoch and orbital period: T_0 = 2459597.2866 and P = 0.80625424 d. Figure 2 shows the folded light curves plotted from orbital phase -0.6 to 0.6, with negative phase defined as $(\varphi - 1)$. The error of a single observation ranged from 5 to 10 mmag. The check star magnitudes were plotted and inspected each night, but no significant variability was found (see bottom of Figure 2). The light curve properties for each passband are given in Table 3 (Min I, Min II, Max I, Max II, Δm). The observations can be accessed from the AAVSO International Database (Kafka 2017).

3. Period analysis and ephemerides

New times of minima were calculated from the observations using the Kwee and van Woerden (1956) method. The Heliocentric Julian Dates (HJD) of these minima are reported in Table 4, along with an additional 19 minima times found in the literature. The initial linear ephemeris for this period study was taken from Diethelm (2009) and is given by:

$$\text{HJD Min I} = 245399.588 + 0.806257\ E. \quad (1)$$

The differences between the observed and predicted minima times using this ephemeris are tabulated in the O−C column of Table 4. Before computing new ephemerides, the following three outliers were removed from the data set: cycles 279.5, 1171.5, and 1842.5. A least-squares solution of the Equation 1 residuals gives the following new linear ephemeris:

$$\text{HJD Min I} = 2453399.5890\,(2) + 0.80625721\,(4)\ E. \quad (2)$$

The top panel of Figure 3 shows the residuals (dots) calculated from Equation 1, with the dashed line the linear best-fit of Equation 2. The coefficient of determination from this regression, $R^2 = 0.080$, is quite low, indicating this ephemeris may not be reliable in predicting future primary eclipses. The orbital period may be undergoing a long-term linear period change, which is most often attributed to mass transfer or angular momentum loss due to magnetic braking. A second least-squares solution of the Equation 1 residuals gives the following quadratic ephemeris:

$$\text{HJD Min I} = 2453399.5896\,(1)$$
$$+ 0.80625824\,(6)\ E - 1.7\,(1) \times 10^{-10}\ E^2. \quad (3)$$

The coefficient of determination from this regression is considerably higher compared to the linear fit, with a value of $R^2 = 0.518$. The middle panel of Figure 3 shows the O−C residuals (dots) from Equation 1 and the quadratic ephemeris fit from Equation 3 (dashed line). The bottom panel of Figure 3 displays the residuals from the quadratic fit. The negative

quadradic coefficient of Equation 3 indicates the orbital period is slowly decreasing. The rate of period change was calculated using the following equation:

$$dP/dt = (2Q/P) \cdot 365.24. \quad (4)$$

The orbital period is decreasing at a rate of $-1.55\,(9) \times 10^{-7}$ d yr^{-17}, or about 1.34 seconds per century.

4. Light curve analysis

4.1. Color, temperature, spectral type, and absolute magnitude

There are no spectroscopic measurements available for this binary, therefore an estimate of the primary star's effective temperature was determined from the photometric color data. For measuring color change and Roche modeling, the large number of photometric observations were binned in both phase and magnitude. This resulted in 125 normal points for each color with a phase width of 0.008. The phases and magnitudes of the observations in each bin were averaged. For color index, the binned r' magnitudes were then subtracted from the linearly interpolated g' magnitudes. The binned points of the r' light curve and the (g' − r') color index are shown in Figure 4 (bottom panel). The large difference in eclipse depths indicates the primary and secondary stars have very different temperatures. Over one orbital period, these temperature differences cause the large color change seen in Figure 4. The color index ranged from (g' − r') = 0.699 ± 0.003 at primary minimum to (g' − r') = 0.293 ± 0.004 at secondary minimum. Even though the eclipses are not quite total, a reasonable estimate for the primary star's effective temperature can be found by using the observed color at secondary eclipse (φ = 0.5). At this orbital phase the secondary star's contribution to the total system light is at a minimum. The color excess for this system is E(g' − r') = 0.11 ± 0.06 and E(B − V) = 0.097 ± 0.05. These values were determined from dust maps based on Pan-STARRS1 and 2MASS photometry and Gaia parallaxes (Green *et al.* 2018). Subtracting the color excess from the observed color at secondary eclipse gives the primary star's approximate intrinsic color, (g' − r')$_0$ = 0.18 ± 0.06. The effective temperature and spectral type for this color are T_{eff} = 6848 ± 187 K and F2, respectively (Pecaut and Mamajek 2013). This effective temperature is in good agreement with a value determined using Gaia EDR3 data, T_{eff} = 6781 ± 105 K (Anders *et al.* 2022). The absolute visual magnitude at quadrature (φ = 0.25), M_v = 3.1 ± 0.3, was calculated using the Gaia distance (d = 367 ± 42 pc) and the apparent visual magnitude corrected for extinction (m_v = 10.9 ± 0.2) (Bailer-Jones *et al.* 2021; Gaia Collaboration *et al.* 2016, 2018).

4.2. Synthetic light-curve modeling

For light curve modeling, 125 normal points were created from observations in the V, g', r', and i' passbands (see section 4.1). On average each normal point was formed from eight observations. The normal points were converted from magnitudes to relative flux for light curve modeling. Preliminary fits to each light curve were obtained using the BINARY MAKER 3.0 program (BM3; Bradstreet and Steelman 2002). The effective temperature of the primary star was fixed at 6848 K and
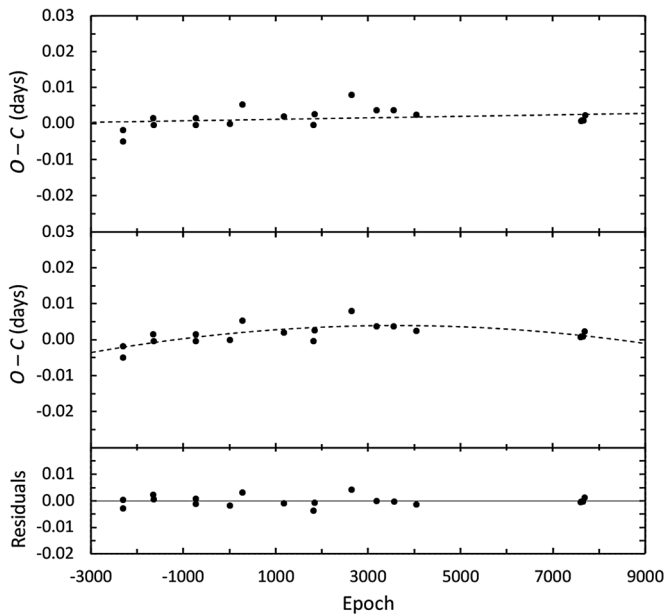
Figure 3. The top panel shows the O – C residuals (dots) from Equation 1 with the dashed line the linear best–fit of Equation 2. The middle panel shows the quadratic best–fit of Equation 3 (dashed line) to the Equation 1 residuals. The bottom panel shows the residuals from the quadratic fit.
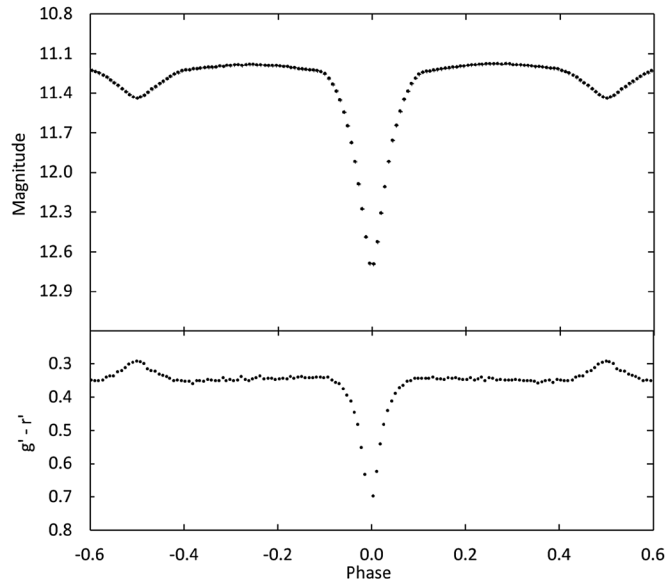

Figure 4. Light curve of the binned Sloan r' passband observations in standard magnitudes (top panel). The observations were binned with a phase width of 0.008. The errors for each binned point are approximately the size of the plotted points. The (g' – r') colors were calculated by subtracting the linearly interpolated binned g' and r' magnitudes.

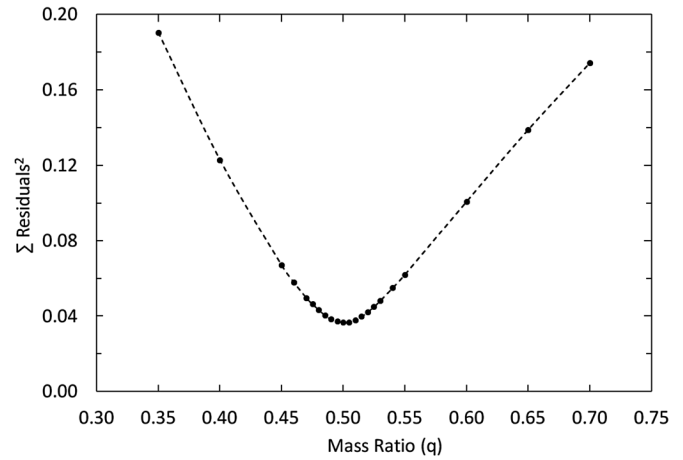Figure 5. Results of the q-search showing the relation between the sum of the residuals squared and the mass ratio q.

Table 5. Results derived from light-curve modeling.

Parameter	Mode-2: No Spots	Mode-2: Spot	Mode-5: Spot
i (°)	86.57 ± 0.12	86.70 ± 0.08	86.58 ± 0.09
T_1 (K)	[1]6848	[1]6848	[1]6848
T_2 (K)	4801 ± 29	4806 ± 22	4809 ± 20
Ω_1	3.803 ± 0.020	3.752 ± 0.015	3.806 ± 0.018
Ω_2	2.904 ± 0.006	2.906 ± 0.016	[2]2.876
$q(M_2 / M_1)$	0.511 ± 0.002	0.510 ± 0.005	0.500 ± 0.005
$L_1/(L_1+L_2)$ (V)	0.841 ± 0.006	0.845 ± 0.005	0.838 ± 0.005
$L_1/(L_1+L_2)$ (g')	0.871 ± 0.006	0.877 ± 0.005	0.868 ± 0.005
$L_1/(L_1+L_2)$ (r')	0.810 ± 0.007	0.815 ± 0.006	0.807 ± 0.005
$L_1/(L_1+L_2)$ (i')	0.773 ± 0.007	0.777 ± 0.006	0.770 ± 0.006
r_1 side	0.323 ± 0.002	0.318 ± 0.001	0.315 ± 0.001
r_2 side	0.309 ± 0.002	0.311 ± 0.005	0.313 ± 0.001
x_1 (V)	0.62 ± 0.05	0.68 ± 0.03	0.63 ± 0.03
x_1 (g')	0.77 ± 0.05	0.81 ± 0.03	0.79 ± 0.03
x_1 (r')	0.41 ± 0.06	0.47 ± 0.04	0.42 ± 0.04
x_1 (i')	0.13 ± 0.07	0.19 ± 0.05	0.12 ± 0.05
x_2 (V)	0.84 ± 0.08	0.89 ± 0.06	0.84 ± 0.06
x_2 (g')	0.88 ± 0.10	0.96 ± 0.08	0.88 ± 0.07
x_2 (r')	0.69 ± 0.06	0.74 ± 0.05	0.69 ± 0.05
x_2 (i')	0.41 ± 0.07	0.45 ± 0.06	0.41 ± 0.06
Residuals	0.00021	0.00018	0.00019
Star 2		Cool Spot	Cool Spot
colatitude (°)	—	79 ± 13	79 ± 13
longitude (°)	—	330 ± 4	329 ± 4
spot radius (°)	—	12 ± 4	12 ± 4
temp. factor	—	0.85 ± 0.11	0.86 ± 0.11

Note: The errors in the stellar parameters result from the least–squares fit to the model. The actual uncertainties are considerably larger. The subscripts 1 and 2 refer to the star being eclipsed at primary and secondary minimum, respectively. [1] Assumed. [2] Calculated.
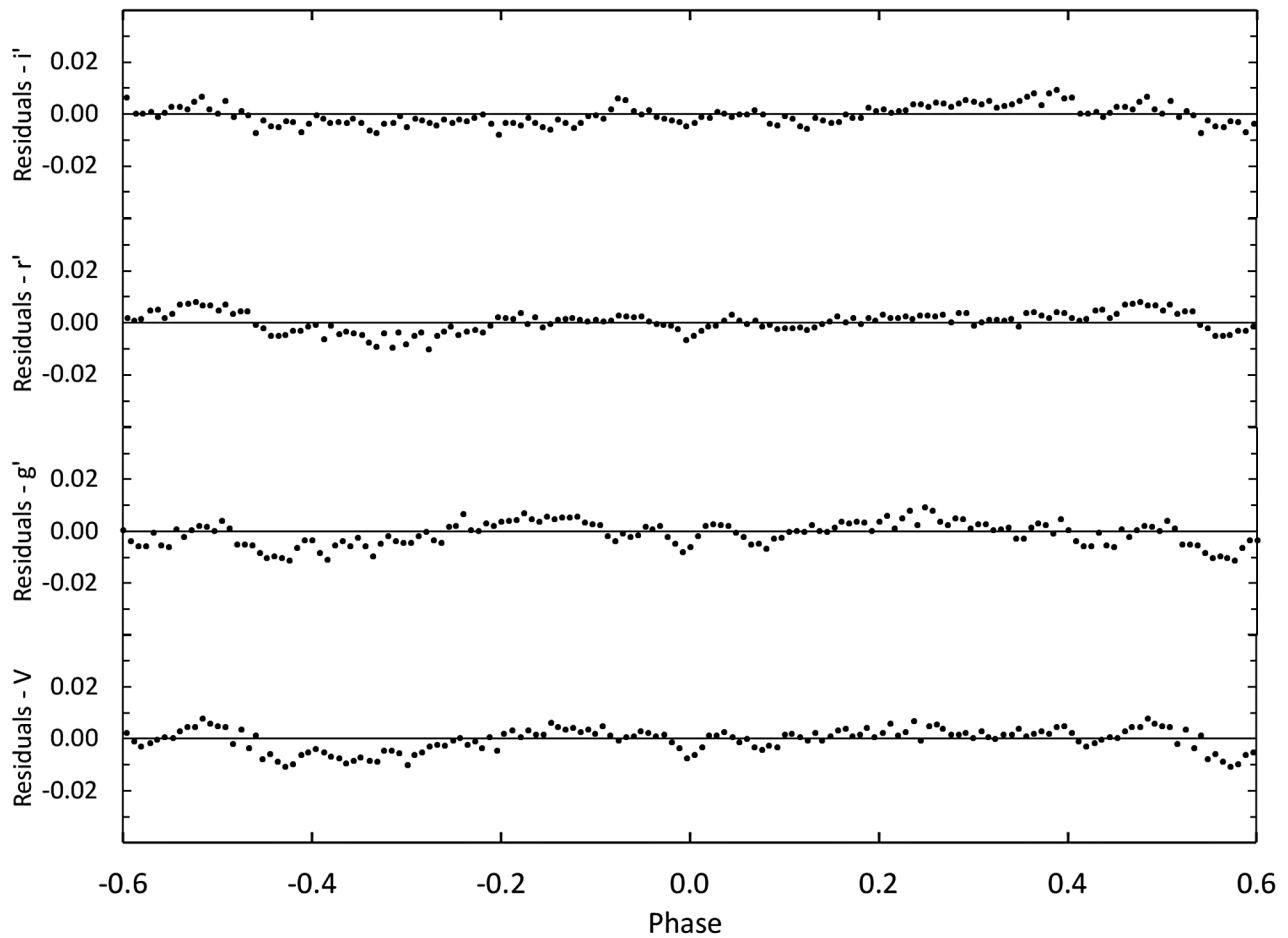
Figure 6. The residuals for the best-fit Mode-2 WD spotless model. Error bars are omitted from the points for clarity.

standard convective parameters were used for gravity darkening and bolometric albedo. Linear limb darkening coefficients were taken from van Hamme's (1993) tabular values. The other parameters—inclination, mass ratio, potentials, and secondary star temperature—were adjusted in sequence until a good fit was obtained between the synthetic light curves and the observations for each passband. The parameters resulting from each light curve fit were averaged. These averages were used as the initial input parameters for the computation of a simultaneous 4-color light curve solution using the 2015 version of the Wilson-Devinney (WD) program (Wilson and Devinney 1971; van Hamme and Wilson 1998).

The observed light curves display a deep partial primary eclipse, a shallow secondary minimum, and small changes in light outside of the eclipses (see Figure 2). This light curve morphology is characteristic of an Algol-type eclipsing binary. The components are often in a detached configuration with spherical or slightly elliptical components, but some are semidetached with one star filling its Roche lobe. Since the configuration of this system is unknown, the WD program was configured to Mode-2 for detached binaries. For modeling, the Kurucz (2002) stellar atmosphere radiation formulas were utilized, and the primary star's effective temperature was fixed at $T_1 = 6848$ K (see section 4.1). The subscripts 1 and 2 refer to the hotter and cooler components, respectively. Since both component temperatures are less than 7500 K, the internal energy

transfer to the surface is due to convection rather than radiative transfer. Gravity brightening and bolometric albedo were therefore set to their standard convective values for modeling, $g_1 = g_2 = 0.32$ (Lucy 1968) and $A_1 = A_2 = 0.5$ (Ruciński 1969), respectively. The adjustable parameters include the inclination (i), mass ratio ($q = M_2/M_1$), potentials (Ω_1, Ω_2), secondary star effective temperature (T_2), band-specific luminosities for each wavelength (L), linear limb-darkening coefficients (x1, x2), and third light (l). The mass ratio cannot be determined directly, since radial velocity measurements are not available for this system. A reliable q value can also be obtained from a photometric solution, but only if the eclipses are total (Wilson 1978; Terrell and Wilson 2005). Since the eclipses are partial, a q-search was necessary to find the most likely mass ratio. A series of WD solutions were completed with each using a fixed mass ratio that ranged from 0.35 to 0.70. The relation between the $\Sigma \text{Residuals}^2$ and the q values is shown in Figure 5. The minimum residual value was located at q = 0.502. This value was used as the starting mass ratio for subsequent solution iterations where the mass ratio was an adjustable parameter. The final Mode-2 solution parameters are shown in column 2 of Table 5. The residuals from this solution (see Figure 6) show a small loss of light in each color between orbital phase 0.5 and 0.8. This type of asymmetry is often attributed to spotting in the photospheres of low mass stars. To fit the asymmetry, several spot configurations were modeled with BM3.
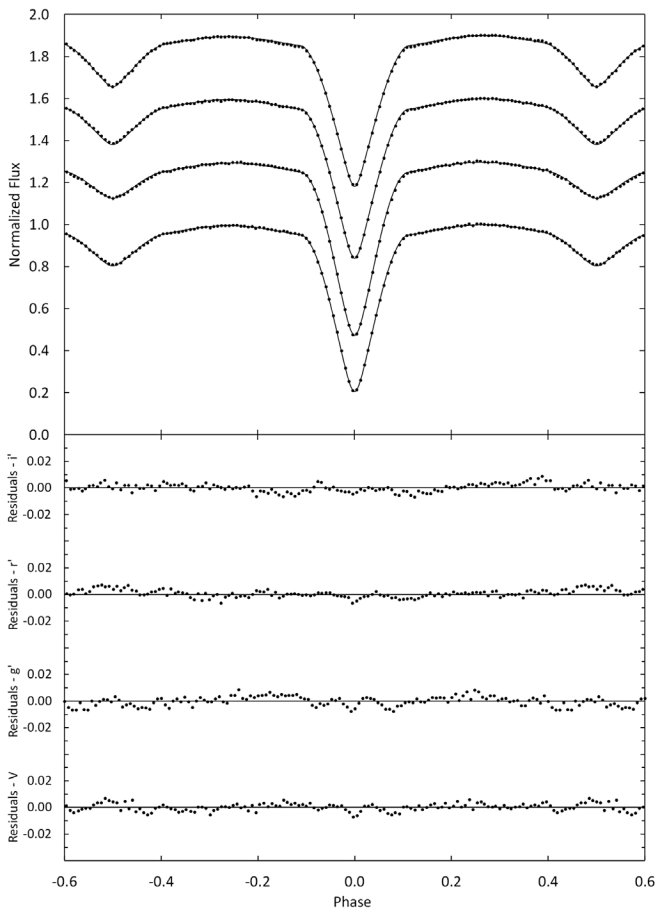
Figure 7. Comparison between the WD spotted best-fit model (solid curve) and the observed normalized flux curve. From top to bottom, the passbands are i', r', g', and V. Each light curve is offset by 0.30 for this combined plot. The residuals are shown in the bottom panel. Error bars are omitted from the points for clarity.

Table 6. Provisional absolute parameters.

Parameter	Symbol	Value
Stellar masses	M_1 ($M_\odot$)	1.47 ± 0.04
	M_2 ($M_\odot$)	0.73 ± 0.02
Semi–major axis	a ($R_\odot$)	4.74 ± 0.03
Mean stellar radii	R_1 ($R_\odot$)	1.49 ± 0.01
	R_2 ($R_\odot$)	1.51 ± 0.03
Bolometric magnitude	$M_{bol,1}$	3.1 ± 0.1
	$M_{bol,2}$	4.6 ± 0.2
Stellar luminosity	L_1 ($L_\odot$)	4.4 ± 0.4
	L_2 ($L_\odot$)	1.1 ± 0.2
Absolute visual magnitude	$M_{V,1}$	3.2 ± 0.1
	$M_{V,2}$	5.2 ± 0.2
Surface gravity	$\log g_1$ (cgs)	4.26 ± 0.01
	$\log g_2$ (cgs)	3.95 ± 0.01

Note: The calculated values in this table are provisional. Radial velocity observations are necessary for direct determination of M_1, M_2, and a.
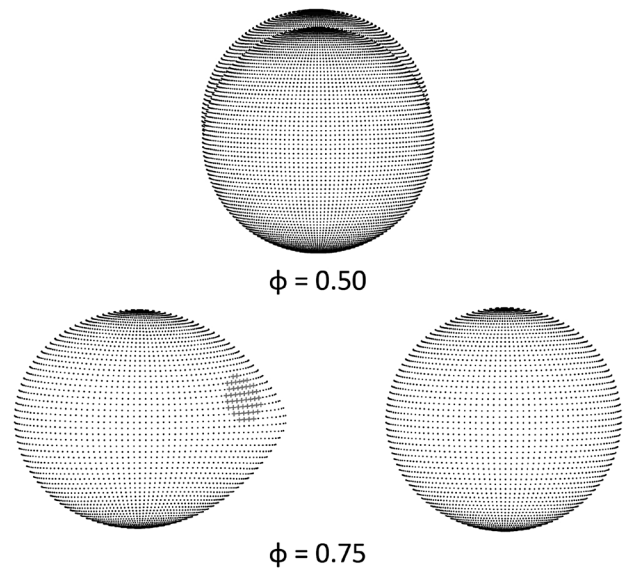

φ = 0.50

φ = 0.75

Figure 8. Roche lobe surfaces of the best–fit WD spot model showing spot locations. The orbital phase is shown below each diagram.
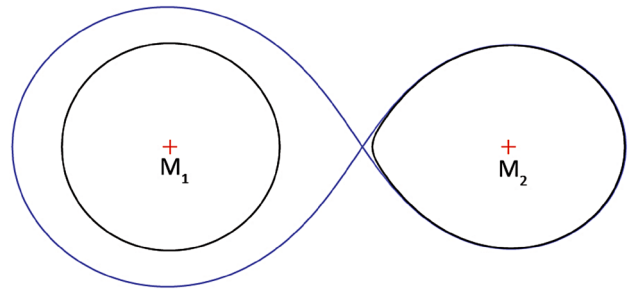

Figure 9. Roche configuration of BO Lep in the orbital plane. The blue line denotes the critical lobe and the black lines the potential surfaces of the two stars for the Mode-2 detached solution.
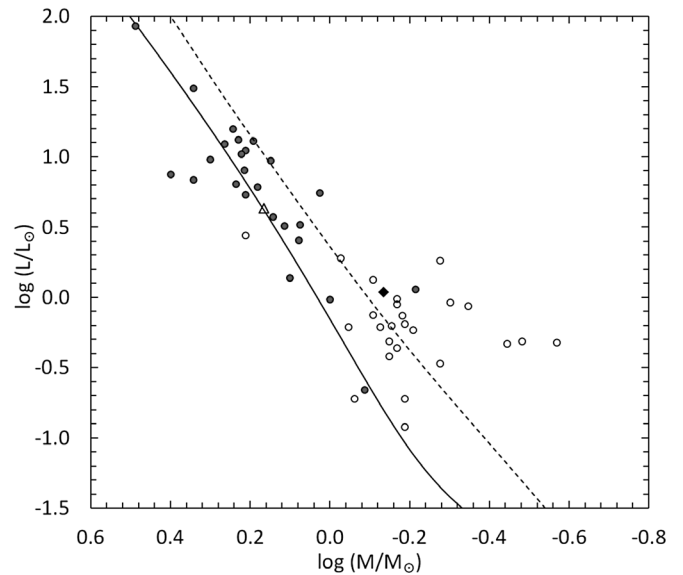

Figure 10. Positions of both components of BO Lep on the Mass-Luminosity diagram of 25 semidetached NCB binaries with well-determined parameters. Filled circles are the primary stars and open circles the secondary stars. The triangle and the diamond are the primary and the secondary of BO Lep, respectively. Solid and dotted lines refer to ZAMS and TAMS, respectively (Tout *et al.* 1996).

The spot parameters, latitude, longitude, spot size and temperature factor were adjusted until the asymmetry was minimized. The best-fit spot parameters were then incorporated into a new Mode-2 WD model. The final solution parameters for the WD spot model are shown in column 3 of Table 5.

The Mode-2 solutions resulted in a semidetached configuration with the cooler less massive secondary star nearly filling its Roche lobe. A final solution was therefore attempted with the WD program set to Mode-5. This mode is often used for semidetached Algol systems. The secondary star's potential (Ω_2) is not adjustable in this mode since it is constrained to exactly fill its Roche lobe during solution iterations. The best-fit final parameters for this solution are shown in column 4 of Table 5. The two sets of solution parameters (Mode-2 and Mode-5) are mostly the same within the margin of errors. The only exceptions are small differences in Ω_2 and q, which is not unexpected given the constraint placed on the secondary component's potential in Mode-5. Figure 7 displays the normalized light curves overlaid by the synthetic Mode-5 solution curves (solid line), with the residuals in the bottom panel. The residuals were reduced by 10% compared to the spotless model. A graphical representation of the spotted model is shown in Figure 8. It should be noted that throughout the solution process, the third-light corrections were negligibly small and often negative. This result likely rules out a bright third body in the system but does not eliminate the possibility for a low luminosity red or brown dwarf star.

5. Discussion

Spectroscopic observations are not available for the direct determination of the orbital and stellar parameters, but provisional values can be estimated using the photometric solution's mass ratio and the mass of one component of the binary. The primary components of Algol systems are typically main sequence stars whose masses can be estimated from their spectral type. Using the primary star's effective temperature, a provisional mass of $M_1 = 1.47 \pm 0.04 \, M_\odot$ was interpolated from Table 5 of Pecaut and Mamajek (2013). Combining this mass with the mass ratio gives a secondary mass of $M_2 = 0.73 \pm 0.02 \, M_\odot$. Applying Kepler's Third Law gives a distance of $4.74 \pm 0.03 \, R_\odot$ between the mass centers of the two stars. The bolometric magnitudes and luminosities were calculated using the solar values $T_{eff\odot} = 5771.8 \pm 0.7 \, K$ and $M_{bol\odot} = 4.74$. The bolometric corrections, $BC_{V1} = -0.004$ for the primary star and $BC_{V1} = -0.390$ for the secondary, were interpolated from Table 5 of Pecaut and Mamajek (2013). The absolute visual magnitudes were computed using these bolometric corrections. All the provisional stellar parameters are collected in Table 6. A distance of $377 \pm 70 \, pc$ was derived based on this system's visual luminosity, the apparent magnitude, and interstellar extinction ($A_V = 0.30 \pm 0.16$). This is consistent with the distance determined from the Gaia parallax (367-pc).

The observed light curves and the photometric solution indicate BO Lep is a semidetached binary where the less massive secondary star fills (or nearly fills) its Roche lobe while the primary star is inside its lobe. The filling factor measures how close the stars are to filling their respective Roche lobes. The filling factor of the primary star is defined as $f_1 = R_1 / R_L$,

where R_1 is the radius of the primary and R_L is the volume radius of the Roche lobe calculated using Eggleton's (1983) formula,

$$\frac{R_L}{a} = \frac{0.49q^{\frac{2}{3}}}{0.6q^{\frac{2}{3}} + \ln\left(1 + q^{\frac{1}{3}}\right)} \, , \qquad (5)$$

where a is the distance separating the mass centers and q the mass ratio. Using the Mode-2 solution radii, the filling factor for the primary star is 72%. The secondary filling factor, 99%, was calculated using a similar equation for R_L / a. Figure 9 shows the Roche surfaces with the nearly filled secondary lobe. Semidetached systems with orbital periods of less than one day and with a large filling factor primary star are described as near-contact binaries (NCB) (Yakut and Eggleton 2005). Figure 10 shows a mass luminosity diagram (M-L) of the components of 25 NCBs with well determined parameters (Yakut and Eggleton 2005). Included in this diagram are the components of BO Lep, the zero-age main sequence line (ZAMS), and the terminal-age main sequence line (TAMS). The NCB primary stars are mostly located along the ZAMS, which supports the assignment of this classification to the primary component of BO Lep. The secondaries are mostly close to or above the TAMS, which means these stars have evolved. The secondary of BO Lep is larger and more luminous than main sequence stars of the same mass, and its location above the TAMS indicates it is also an evolved star.

In the current epoch, BO Lep consists of a less massive but more evolved secondary star, and a more massive but less evolved primary. Theoretical modeling indicates NCBs and contact binaries (CB) form from detached young cool stars with initial orbital periods of about two days (Stepień and Kiraga 2013; Stepień 2011). As the primary star begins to evolve near the end of its main sequence lifetime, combined with mass and angular momentum loss over that same period, Roche lobe overflow will eventually occur. Mass transfer will then cause a reversal in the mass ratio, forming either a CB or NCB. BO Lep is currently at the NCB stage of its evolution. From the period analysis, the downward parabolic trend in the O−C diagram indicates a decreasing orbital period, which implies a nonconservative mass-loss process. For low mass stars this process could result from magnetic braking which is caused by a coupling between the magnetic field and the stellar winds. Magnetic braking will cause a loss of mass and angular momentum that would decrease the orbital period and shrink the orbit. The spot modeled on the secondary star supports current magnetic activity. Conservative mass transfer from the less massive star to the more massive component will have the opposite effect, causing a continuously increasing orbital period and an expanding orbit. The Mode-2 photometric solution indicates the secondary may only be marginally in contact with the Roche surface, thus limiting significant matter transfer through the L_1 point. Due to the proximity of the two stars, a significant mass transfer rate would cause the matter stream to directly impact the primary star, forming a hot spot. The excess light from this spot would form a noticeable hump in the light curves. This asymmetry is not seen and is another indication that mass transfer is presently not active or is occurring at a low rate. It is also possible the decreasing period results from

a combination of mass transfer and wind-driven mass loss. In semidetached systems, these two mechanisms may be strongly competitive (Nanouris *et al.* 2011, 2015; Erdem and Öztürk 2014). Whether BO Lep evolves into a contact binary or an Algol binary will depend on which one of these two mechanisms dominates.

6. Conclusions

The acquisition of precision photometric observations for the eclipsing binary BO Lep resulted in complete light curves in the V, g', r', and i' bands and six new minimum timings. The light curves displayed deep primary and shallow secondary eclipses. Photometric light curve solutions using the WD program found a semidetached configuration with a lower mass secondary star filling its Roche lobe, a mass ratio of q = 0.510, and an orbital inclination of i = 86.6°. The primary component is a main sequence star with a spectral type of F2 and an evolved K3 secondary star. A cool spot on the secondary was included in the final Roche model to address an asymmetry in the light curves. Provisional stellar properties were computed based on the assumption that the primary star has a "normal" main sequence mass for its spectral type. A period analysis resulted in updated ephemerides and revealed an orbital period that is decreasing. This period change results from magnetic braking or a combination of magnetic braking and mass transfer. This NCB will eventually evolve into a contact or an Algol-type binary. A spectroscopic study of this system is required to confirm and update the stellar masses presented in this study and to provide a revised spectral type for the primary star.

7. Acknowledgements

References

Anders, F., *et al.* 2022, *Astron. Astrophys.*, **658A**, 91.
Bailer-Jones, C. A. L., Rybizki, J., Fouesneau, M., Demleitner, M., and Andrae, R. 2021, *Astron. J.*, **161**, 147.
Bradstreet, D., and Steelman, D. 2002, *Bull. Amer. Astron. Soc.*, **34**, 1224.
Diethelm, R. 2009, *Inf. Bull. Var. Stars*, No. 5894, 1.
Diethelm, R. 2011, *Inf. Bull. Var. Stars*, No. 5960, 1.
Diethelm, R. 2012, *Inf. Bull. Var. Stars*, No. 6029, 1.
Diethelm, R. 2013, *Inf. Bull. Var. Stars*, No. 6042, 1.
Drake, A., *et al.* 2014, *Astrophys. J., Suppl. Ser.*, **213**, 9.
Eggleton, P. P. 1983, *Astrophys. J.*, **268**, 368.
Erdem, A., and Öztürk, O. 2014, *Mon. Not. Roy. Astron. Soc.*, **441**, 1166.
Gaia Collaboration, *et al.* 2016, *Astron. Astrophys.*, **595A**, 1.
Gaia Collaboration, *et al.* 2018, *Astron. Astrophys.*, **616A**, 1.
Gaia Collaboration, *et al.* 2021, *Astron. Astrophys.*, **649A**, 1.
Green, G. M., *et al.* 2018, *Mon. Not. Roy. Astron. Soc.*, **478**, 651.
Henden, A. A., *et al.* 2015, AAVSO Photometric All-Sky Survey, data release 9, (https://www.aavso.org/apass).
Kafka, S. 2017, Variable star observations from the AAVSO International Database (https://www.aavso.org/aavso-international-database).
Kurucz, R. L. 2002, *Baltic Astron.*, **11**, 101.
Kwee, K. K., and van Woerden, H. 1956, *Bull. Astron. Inst. Netherlands*, **12**, 327.
Lucy, L. B. 1968, *Astrophys. J.*, **151**, 1123.
Mirametrics. 2015, Image processing, visualization, data analysis (https://www.mirametrics.com).
Nanouris, N., Kalimeris, A., Antonopoulou, E., and Rovithis-Livaniou, H. 2011, *Astron. Astrophys.*, **535A**, 126.
Nanouris, N., Kalimeris, A., Antonopoulou, E., and Rovithis-Livaniou, H. 2015, *Astron. Astrophys.*, **575A**, 64.
Papageorgiou, Athanasios, Catelan, Márcio, Christopoulou, Panagiota-Eleftheria, Drake, Andrew J., and Djorgovski, S. G. 2018, *Astrophys. J., Suppl. Ser.*, **238**, 4.
Pojmański, G. 2002, *Acta Astron.*, **52**, 397.
Pecaut, M. J., and Mamajek, E. E. 2013, *Astrophys. J., Suppl. Ser.*, **208**, 9. (http://www.pas.rochester.edu/~emamajek/EEM_dwarf_UBVIJHK_colors_Teff.txt).
Ruciński, S. M. 1969, *Acta Astron.*, **19**, 245.
Stępień, K., 2011, in *Magnetic Stars*, eds. I. I. Romanyuk, D. O. Kudryatsev, Special Astrophys. Obs., Nizhny Arkhyz, 86.
Stępień, K., and Kiraga, M. 2013, *Acta Astron.*, **63**, 239.
Strohmeier, W. 1967, *Inf. Bull. Var. Stars*, No. 195, 1.
Terrell, D., and Wilson, R. E. 2005, *Astrophys. Space Sci.*, **296**, 221.
Tout, C. A., Pols, O. R., Eggleton, P. P., and Han, Z. 1996, *Mon. Not. Roy. Astron. Soc.*, **281**, 257.
van Hamme, W. 1993, *Astron. J.*, **106**, 2096.
van Hamme, W., and Wilson, R. 1998, *Bull. Amer. Astron. Soc.*, **30**, 1402.
Watson, C., Henden, A. A., and Price, C. A. 2014, AAVSO International Variable Star Index VSX (Watson+, 2006–2014, https://www.aavso.org/vsx).
Woźniak, P. R., *et al.* 2004, *Astron. J.*, **127**, 2436.
Wilson, R. E. 1978, *Astrophys. J.*, **224**, 885.
Wilson, R. E., and Devinney, E. J. 1971, *Astrophys. J.*, **166**, 605.
Yakut, K., and Eggleton, P. P. 2005, *Astrophys. J.*, **629**, 1055.
Zasche, P., Uhlar, R., Kucakova, H., Svoboda, P., and Masek, M. 2014, *Inf. Bull. Var. Stars*, No. 6114, 1.